Characteristics of Landfalling Atmospheric Rivers Inferred from Satellite Observations over the Eastern North Pacific Ocean

SERGEY Y. MATROSOV

Cooperative Institute for Research in Environmental Sciences, University of Colorado, and NOAA/Earth System Research Laboratory, Boulder, Colorado

ABSTRACT

Narrow elongated regions of moisture transport known as atmospheric rivers (ARs), which affect the West Coast of North America, were simultaneously observed over the eastern North Pacific Ocean by the polar-orbiting *CloudSat* and *Aqua* satellites. The presence, location, and extent of precipitation regions associated with ARs and their properties were retrieved from measurements taken at 265 satellite crossings of AR formations during the three consecutive cool seasons of the 2006–09 period. Novel independent retrievals of AR mean rain rate, precipitation regime types, and precipitation ice region properties from satellite measurements were performed. Relations between widths of precipitation bands and AR thicknesses (as defined by the integrated water vapor threshold of 20 mm) were quantified. Precipitation regime partitioning indicated that "cold" precipitation with a significant amount of melting precipitating ice and "warm" rainfall conditions with limited or no ice in the atmospheric column were observed, on average, with similar frequencies, though the cold rainfall fraction had an increasing trend as AR temperature decreased. Rain rates were generally higher for the cold precipitation regime. Precipitating ice cloud and rainfall retrievals indicated a significant correlation between the total ice amounts and the resultant rain rate. Observationally based statistical relations were derived between the boundaries of AR precipitation regions and integrated water vapor amounts and between the total content of precipitating ice and rain rate. No statistically significant differences of AR properties were found for three different cool seasons, which were characterized by differing phases of El Niño–Southern Oscillation.

1. Introduction

The term atmospheric river (AR) is usually applied to long and relatively narrow bands of enhanced water vapor transport (e.g., Zhu and Newell 1998; Ralph et al. 2004). ARs are often associated with cold fronts of extratropical cyclones and play a significant role in the global water cycle, being responsible for much of the meridional moisture transport in the atmosphere. Landfalling ARs are important factors affecting regional weather and climate along the West Coast of the United States as they often are associated with heavy rainfall, which can result in widespread flooding (e.g., Leung and Qian 2009; Dettinger 2011; Ralph et al. 2006, 2010; Lavers et al. 2011). Precipitation including both rainfall and snowfall associated with landfalling atmospheric river events is also crucial for California's water supply (e.g., Guan et al. 2010).

While the importance of the ARs for water cycle budgets is widely recognized, our current level of understanding of AR events needs improvement. Experimental and theoretical studies under the multiagency project named Calwater (http://www.esrl.noaa.gov/psd/calwater/) are aimed at closing some gaps in our scientific knowledge about these events. One objective of these studies is related to assessing how well ARs are represented in climate models and how their properties vary. The Calwater research hypotheses suggest that the representation of clouds in AR formations in current versions of global and regional weather models includes significant errors that can be diagnosed through specialized observations. Specifically, it is believed that quantitative precipitation forecast (QPF) uncertainties result partly from uncertainty in the representation of AR systems offshore in the models (e.g., Ralph et al. 2010). This study deals with novel satellite observations of these systems over the ocean where rainfall associated with ARs is relatively modest compared to orographically enhanced precipitation in the coastal areas.

Corresponding author address: Sergey Matrosov, R/PSD2, 325 Broadway, Boulder, CO 80305.
E-mail: sergey.matrosov@noaa.gov

Spaceborne observations are one important way of obtaining information on AR systems. Over water surfaces, passive satellite measurements of water vapor have been successfully used to identify ARs and their boundaries, which are customarily defined by the vertically integrated water vapor (IWV) amount of 20 mm (e.g., Neiman et al. 2008 and references therein). These measurements were used to estimate the mean width of ARs in a direction perpendicular to moisture plumes at several hundred kilometers (e.g., Ralph et al. (2004). The addition of observations from active spaceborne sensors allows us to gain new insights into AR structures. The combination of passive and active retrievals of geophysical parameters available from measurements conducted by a spaceborne nadir-pointing W-band (~94 GHz) radar aboard the *CloudSat* satellite and the Advanced Microwave Scanning Radiometer for Earth Observing System (EOS) (AMSR-E) aboard the *Aqua* satellite (http://aqua.nasa.gov) flying in formation with *CloudSat* is particularly useful as it provides closely collocated and almost simultaneous estimates of precipitation, cloud (including the ice phase), and water vapor properties.

A number of important issues of AR modeling require observational validations. Such issues include discriminating between different rainfall regimes [i.e., "cold" rain, which often produces the radar bright band (BB) as a result of ice/snow melting, versus "warm" rain, for which cloud liquid to rain autoconversion is the main precipitation process], and water substance partitioning in the cold rain regime, which depends on the choice of the microphysical parameterization scheme (e.g., Jankov et al. 2009). The ability of *CloudSat* spaceborne radar measurements to provide vertical cross sections of atmospheric hydrometeors, which allows for the detailed analysis of rainfall and clouds associated with ARs, is valuable for collecting information needed for model validations and tuning. The main objective of this study was to construct observationally based relations among different characteristics of AR events based on multiyear spaceborne combined measurements by *CloudSat* and *Aqua* satellites, which fly in formation. This satellite measurement combination has an advantage over other spaceborne active–passive combinations (e.g., Tropical Rainfall Measuring Mission precipitation radar and microwave imager), as it is more sensitive to clouds and it covers more northern areas, which are of interest for AR studies.

2. Datasets and methodology

The primary area of interest for this study is the eastern North Pacific Ocean bounded by 55°–20°N and 115°–170°W. There are typically several dozen days per cool season period when AR events affecting the coast are observed in this area. The landfalling precipitating ARs are generally active during this period, which lasts from October to March. The events observed during this period were analyzed in this study.

National Oceanic and Atmospheric Administration (NOAA) researchers P. Neiman and G. Wick (2012 personal communication) maintain a detailed log that lists AR events affecting the U.S. West Coast. This study is focused on AR satellite observations performed during three consecutive cold season periods (2006–07, 2007–08, and 2008–09), and it examines satellite retrievals of AR events listed in the NOAA log.

The three cool season periods considered here were characterized by different phases of El Niño–Southern Oscillation (ENSO), representing both warming and cooling episodes. Oceanic Niño Index (ONI), which is defined by sea surface temperature anomalies (°C) in the Niño-3.4 region (5°N–5°S, 120°–170°W), values were 0.85, −1.35, and −0.6 for the 2006–07, 2007–08, and 2008–09 observations periods, respectively. Conventionally, the ONI values, which are higher than 0.45, represent El Niño conditions, and the ONI values lower than −0.45 correspond to La Niña conditions.

Both *CloudSat* and *Aqua* are part of the A-Train satellite constellation (http://atrain.nasa.gov/), which flies in sun-synchronous orbits with an inclination of 98.14° at an altitude of about 700 km. The orbits repeat themselves approximately every 16 days, and there are about 90 or so satellite crossings of landfalling ARs observed by A-Train sensors over the eastern North Pacific Ocean area of interest per each cold season observation period. Specifically there were 94, 77, and 95 ocean crossings for the 2006–07, 2007–08, and 2008–09 cool seasons, respectively.

While the *CloudSat* main objective was collecting information on clouds, the spaceborne W-band radar proved to also be an effective tool for rainfall retrievals. For each event when *CloudSat* and *Aqua* crossed an AR, retrievals of mean rain rate in a vertical column and ice water content (IWC) profiles were performed using *CloudSat* cloud profiling radar (CPR) measurements of equivalent reflectivity factor Z_e. Since attenuation of W-band signals in liquid hydrometeors is strong, CPR-based rainfall retrieval methods use attenuation effects to obtain information on rain rate (e.g., Matrosov et al. 2008; Haynes et al. 2009). The *CloudSat* rainfall retrieval procedures for AR system rainfall parameters are described in detail by Matrosov (2012), where several characteristic case studies and retrieval validations/comparisons are also shown. Expected uncertainties of estimating rainfall from CPR measurements could be on the order
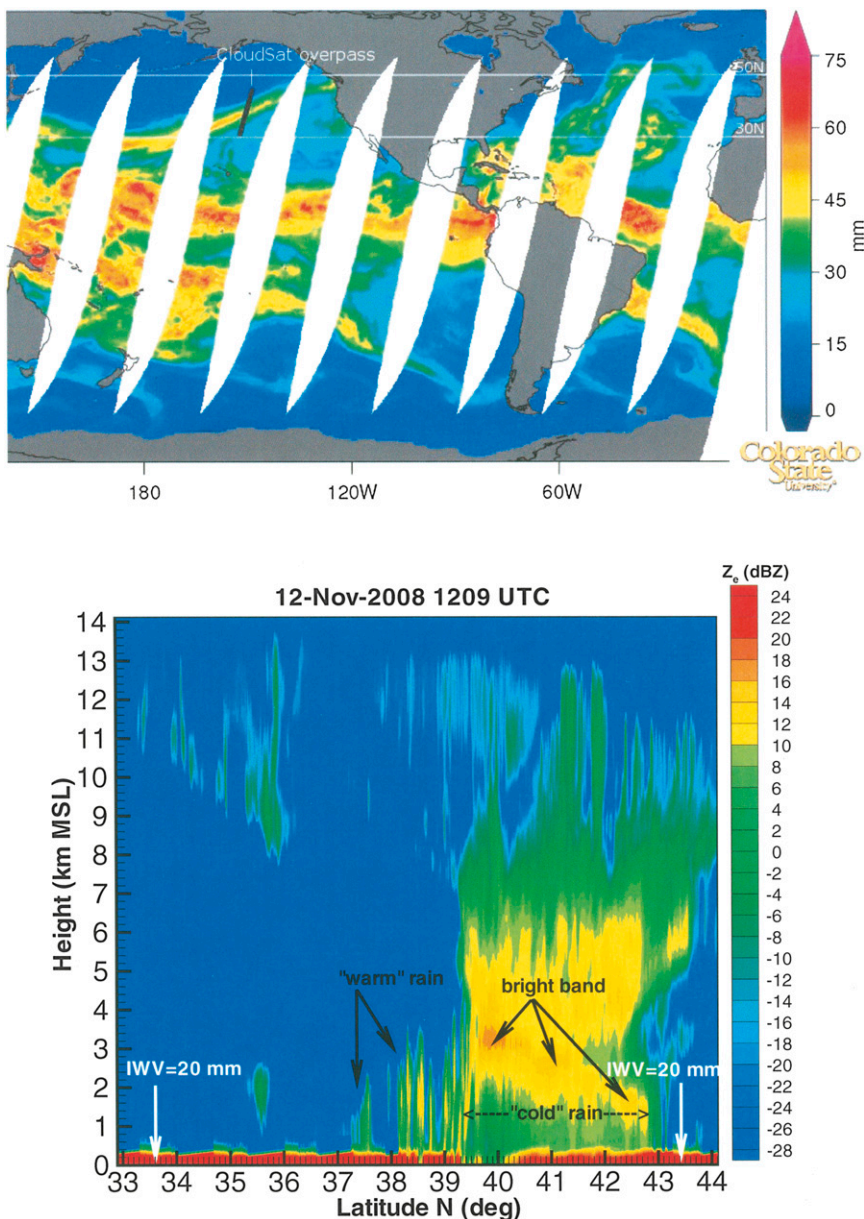
FIG. 1. (top) A *CloudSat–Aqua* AR crossing from 12 Nov 2008 superimposed on an IWV map of AMSR-E based IWV retrievals [the IWV map is courtesy of Colorado State University's (CSU) National Aeronautics and Space Administration (NASA) Making Earth System Data Records for Use in Research Environments (MEASURES) rainfall project]. (bottom) The *CloudSat* CPR reflectivity cross section corresponding to the crossing in the top panel (vertical white arrows mark 20-mm AR boundaries).

of 40%–50% for stratiform brightband rain conditions (e.g., Matrosov 2007). For warm rainfall with lower intensity ($R < 1 \, \mathrm{mm \, h^{-1}}$), retrieval uncertainties could reach 100% or even higher (Haynes et al. 2009).

An example of one such AR crossing during a descending satellite orbit is shown in Fig. 1. According to the *Aqua* AMSR-E-based retrievals for this crossing,

IWV values exceeded the AR boundary threshold of 20 mm along the satellite track between latitudes of about 33.9° and 43.1°N. The CPR reflectivity vertical cross section shows rainfall associated with this AR event between approximately 37.3° and 43.1°N. The BB features are clearly observed for the portion of this rainfall to the north of 39.3°N. The cold rainfall in this

area has extensive regions of precipitating ice/snow observed above the bright band, which approximately identifies the height of the freezing level. The rest of the observed precipitation (i.e., to the south from approximately 39.3°N) represents the warm rain with most of the radar echo coming from altitudes below the freezing level.

The parameters of ice cloud regions [i.e., IWC and its vertical integral—ice water path (IWP)] of AR precipitating systems were retrieved using the absolute values of reflectivities Z_e, which are not affected by signal attenuation in liquid hydrometeors present below these regions. The radar-only approach for IWC/IWP retrievals based on *CloudSat* data (Matrosov and Heymsfield 2008), which accounts for the general nonsphericity of ice particles, is used because approaches that utilize visible and/or infrared (IR) measurements in addition to radar data are generally not applicable to optically thick precipitating cloud systems. The radar-only retrievals, however, remain a viable option for such systems (e.g., Matrosov 1997).

It is important that *CloudSat* rainfall and precipitating cloud ice region parameter retrievals are independent in the sense that CPR measurements from different heights in the atmospheric column are used as input information for ice and rainfall and no a priori assumptions are made about the interdependence of cloud and precipitation parameters, as is often the case for retrievals from passive satellite measurements. Unlike for any other satellite sensor, *CloudSat* CPR provides information on cross sections of AR events in their vertical entirety all the way from cloud tops (at an approximately −29-dBZ CPR sensitivity level) to the surface. *CloudSat* rainfall retrievals are typically available up to a limit of about 20 mm h^{-1}, beyond which the multiple scattering effects overwhelm the radar returns (e.g., Matrosov et al. 2008).

Brightband (BB) features identifiable in CPR data near the freezing level for rainfall, which result primarily from ice/snow melting processes, effectively separate ice and liquid water regions of stratiform precipitating events. Interpolation of identified BB heights and model estimates of freezing level from the European Centre for Medium-Range Weather Forecasts (ECMWF) model are used for areas where the BB signatures are not present. Due to the nadir-pointing CPR measurements, *CloudSat*-based retrievals were performed along the satellite orbit tracks. IWV values and AR boundaries, which are based on the 20-mm IWV threshold, were determined from the *Aqua*-based AMSR-E measurements at an AMSR-E pixel that is closest to the CPR footprint. Altogether, retrieval data for all 265 AR satellite crossings, which occurred during the 2006–07, 2007–08, and 2008–09 cool seasons, were used in this study. More details on specific

retrieval procedures and BB/freezing level identifications using satellite data are given in Matrosov (2012).

3. AR properties estimated from satellite measurements

a. Precipitation regimes observed in AR events

CloudSat measurements indicate that there is rainfall associated practically with all satellite AR crossings over the ocean area of interest to this study. The spatial extent, intensity, and precipitation regime of the observed rainfall, however, vary significantly. Rainfall associated with ARs is sometimes not contiguous, as seen in Fig. 1 (bottom), where there is a small gap in the rain between approximately 37.7° and 38.1°N in an otherwise almost contiguous core rainband, which extends from 37.3° to 43.1°N. CPR data indicate that for all AR crossings analyzed in this study, an average percentage of no-rain intervals in a core rainband associated with atmospheric rivers is about 15%. This percentage varies relatively little with observational period. For the 2006–07, 2007–08, and 2008–09 seasons, for example, the corresponding percentages were approximately 15%, 12%, and 18%, respectively.

While many of the satellite crossings revealed that the rain associated with ARs is either of the cold type or the warm type, a fair amount of observed precipitation was of the "mixed" type when both precipitation regime types were present within one AR crossing. The example in Fig. 1 presents a case of such mixed rain. For this example, the warm rain fraction, defined as the ratio of CPR profiles when the warm rain type is identified to the total number of rain profiles within a given AR crossing, is approximately 30%. Figure 2 shows the statistical distribution histograms of the warm rain fraction for the events observed during each of the three cool seasons (i.e., 2006–07, 2007–08, and 2008–09) separately as well as the composite results for all three seasons. About 40% of all ARs (including the example in Fig. 1) were connected to low-latitude moisture reservoirs primarily to the west of 180° longitude. The remaining 60% of the events were characterized by ARs tapping into such reservoirs to the east of this longitude. The results of rainfall regime partitioning based on the origins of detected ARs are also depicted in Fig. 2.

It can be seen from Fig. 2 that a category of predominately warm (cold) rain [i.e., rain with the warm (cold) rain fraction greater (smaller) than 0.9 (0.1) within one AR crossing] is observed in about 30% (for each category) of the events. Mixed-rain regimes, when for a given crossing both rain type profiles are present in more than 10% of all rainy CPR profiles, are observed in
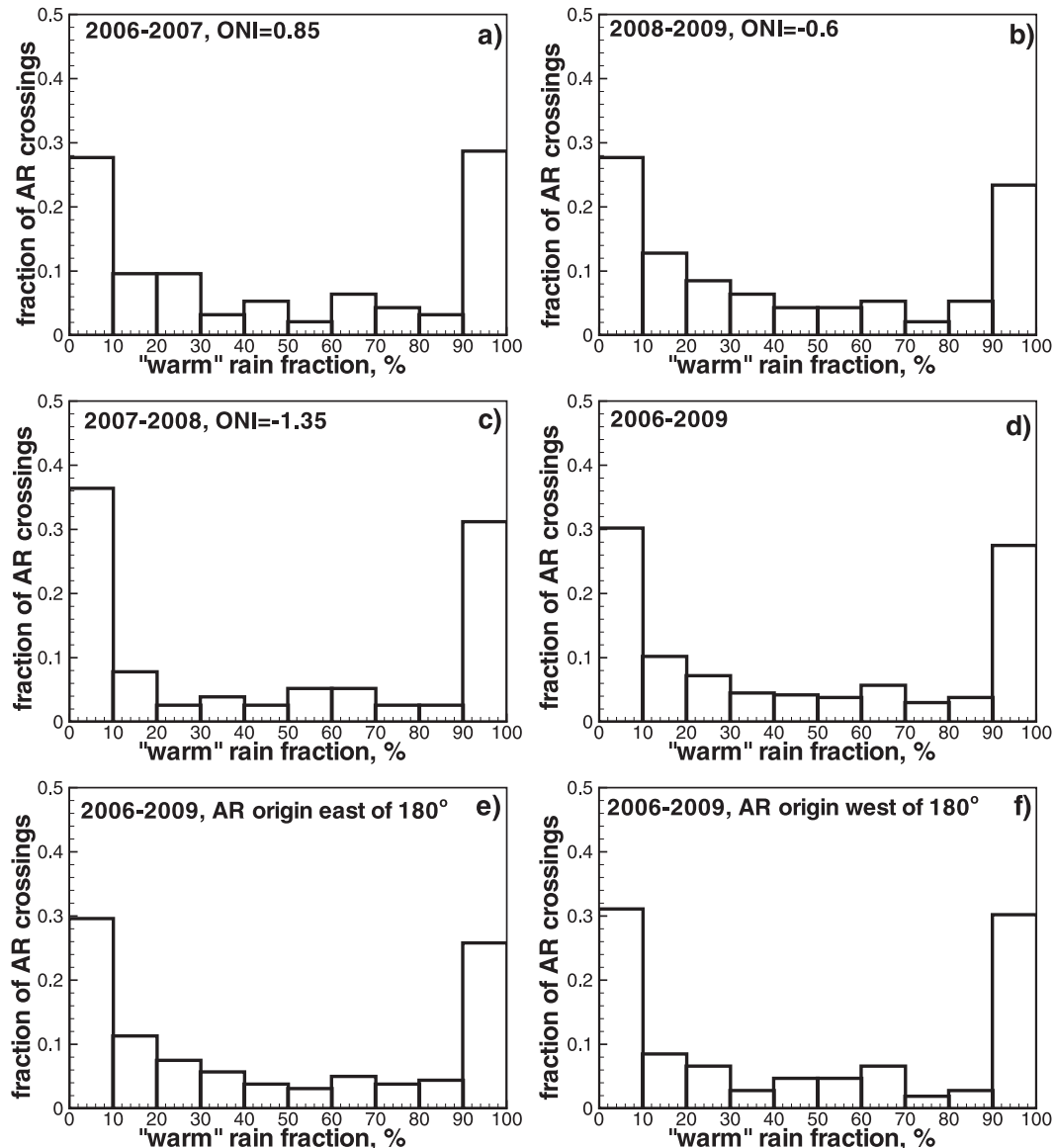
FIG. 2. Histograms of the precipitation regime observed during the satellite AR crossings for the observational (a) 2006–07, (b) 2008–09, and (c) 2007–08 periods, as well as (d) the composite for 2006–09, and the subsets of ARs tapping moisture reservoirs (e) east and (f) west of 180° longitude. The warm rain fraction is defined as the ratio of CPR profiles when the warm rain type is identified to the total number of rain profiles in a crossing.

approximately 40% of the AR events analyzed in this study. There are no statistically significant differences between the results based either on AR origins or for different cool season periods, even though these periods were characterized by quite distinct ONI indices suggesting different phases of ENSO. Overall, the mean warm rain fraction for all the events was about 48%.

The cold rain regimes, which tend to exhibit radar brightband features, were more prevalent for northern AR crossings, which were generally characterized by lower temperature T_m. For the purpose of this study, this temperature is estimated from the ECMWF model output

near the surface, which is coincident with a *CloudSat–Aqua* crossing, and is calculated as a mean value along the given crossing within the AR boundaries. Approximately half of all AR crossings from the dataset considered here were characterized by $T_m > 287.5$ K (i.e., the warmer AR events). As shown in Table 1, for those events the warm rain fraction was about 27%, compared to 67% for the ARs with $T_m \leq 287.5$ K.

The warm rain fraction was also analyzed based on the mean latitudes of satellite AR crossings ϕ_m. While near-surface crossing temperature is on average related to latitude, such analysis is useful for comparison purposes

TABLE 1. Mean warm rain fractions, cloud echo tops, and AR widths (at a 20-mm IWV threshold) for warmer (colder) [southern (northern)] AR crossings. For mean AR temperature and crossing latitudes values, $T_m = 287.5$ K and $\phi_m = 40°$N are median values.

	$T_m > 287.5$ K	$T_m \leq 287.5$ K	$\phi_m < 40°$N	$\phi_m \geq 40°$N
Warm rain fraction (%)	67	27	64	28
Cloud echo top (km MSL)	4.9	7.5	5.1	7.3
AR width (perpendicular to moisture plume, km)	644	625	640	629

since Ralph et al. (2004) stratified their data based on latitude. The median value of mean crossing latitude for events in the current study was about 40°N. As seen from Table 1, for half of the total number of crossings that occurred at latitudes to the south of 40°N the warm rain fraction was about 28% as opposed to 64% for more northern AR crossings.

Table 1 also shows mean cloud-top heights as detected by the CPR and AR widths (in the direction perpendicular to moisture plumes) as estimated from passive microwave retrievals for warmer (colder) and southern (northern) crossings. It can be seen that colder ARs and more northern AR events are generally characterized by thicker precipitating cloud systems with higher tops as measured by the CPR. This is in general agreement with the results of Ralph et al. (2004), who, by analyzing passive measurements from the Geostationary Operational Environmental Satellite (GOES), found higher cloud tops for more northern AR locations.

The variability in AR widths in a direction perpendicular to the moisture plume for different mean temperatures and crossing latitudes (see Table 1) as determined by the 20-mm IWV threshold is not that distinct. AR widths from this study are about 50% larger than those reported in the earlier study by Ralph et al. (2004). One significant reason contributing to such a discrepancy in AR widths is that the Schlüssel and Emery (1990) IWV retrieval algorithm used in this earlier study was found to produce a "dry" bias compared to more modern IWV retrieval algorithms used with passive microwave satellite data (Wick et al. 2008).

Retrieved rain rates R for cold precipitation regimes were noticeably greater than those for warm rainfall. Figure 3 depicts the mean rain rate along the AR crossings as a function of the warm rain fraction in the observed precipitation region. The data are shown for all cool seasons from the entire 2006 to 2009 period. The diminishing rain-rate trend in this figure, as the warm rain fraction increases, is obvious. Table 2 shows the mean values of R for the AR crossings when different precipitation regimes were observed during various observation periods. The data are also stratified based on AR origins. Despite the rain-rate retrieval uncertainty, the difference between the mean values for different rain types in Table 2 is statistically significant since these

values were obtained by averaging the large number of individual retrievals. As for the regime prevalence histograms discussed previously, there is no significant difference in mean rain rates depending on the observation period or AR origins.

The warm (cold) rain detected by *CloudSat* can be considered as belonging to nonbrightband (brightband) rainfall categories that are often used for rainfall classification when employing ground-based centimeter-wavelength radar profilers (e.g., White et al. 2003). However, not all nonbrightband rainfall as classified by such profilers is warm rain. This is because substantial amounts of ice hydrometeors may be present in precipitation, which results in near-surface rain without causing distinct brightband features at centimeter wavelengths even when echo-top heights significantly exceed freezing levels. Since the brightband features near freezing levels in nadir-pointing W-band radar data are primarily caused by attenuation in rainfall below (e.g., Matrosov 2008) as opposed to reflectivity enhancement at centimeter wavelengths, these features may be present in *CloudSat* measurements even for events when bright bands are not clearly defined in the ground-based profiler radar data.

b. Spatial extent of rainbands in ARs over the ocean

Using solely passive microwave retrievals for one season, Ralph et al. (2004) estimated that rainband
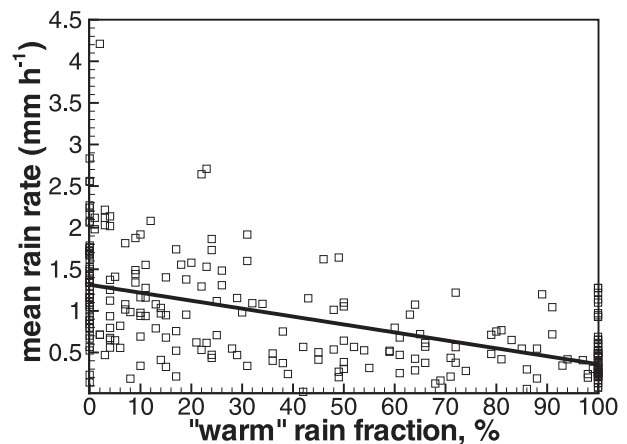

FIG. 3. Mean rain rate as a fraction of warm rain fraction in precipitation observed at AR crossings (2006–09 dataset).

TABLE 2. Mean rain rates in precipitation of different regimes observed at satellite AR crossings during different seasons and based on AR origins.

	"Warm" rain areas (warm rain fraction >90%; mm h^{-1})	"Cold" rain areas (warm rain fraction <90%; mm h^{-1})	"Mixed" rain areas (mm h^{-1})
2006–07 season	0.43	1.68	1.02
2007–08 season	0.49	1.34	1.00
2008–09 season	0.42	1.18	0.92
2006–09 composite	0.45	1.38	0.98
AR origin east of 180° (2006–09)	0.43	1.42	0.92
AR origin west of 180° (2006–09)	0.48	1.39	1.04

widths associated with ARs are narrower than AR widths (for the 20-mm AR boundary threshold) by a factor of about 3. Since active *CloudSat* CPR measurements can generally identify the presence of precipitation more robustly, estimates of ratios of AR widths to rainband widths can be made independently by using passive predictions of AR widths from *Aqua* AMSR-E measurements.

For all A-Train AR overpasses considered in this study, Fig. 4 shows the ratio of the rainband width to the AR width r as a function of the mean value of IWV during a crossing, hereafter denoted as IWV$_m$. Due to the nadir-pointing mode of CPR measurements, IWV$_m$ values and rainband and AR widths for this particular analysis were estimated along the satellite crossing ground tracks. The ratio r varies from about 0.01, corresponding to very narrow rainbands, which usually are represented by only a few CPR profiles, indicating rainfall within AR boundaries, to more than 1.5, when the widths of the rainbands associated with ARs significantly exceeded boundaries set by the 20-mm threshold. If all satellite AR crossings analyzed in this study are considered, the mean value of the ratio r is 0.47 and there is a general tendency for this ratio to decrease with increasing IWV$_m$.

There is also some variability of the rainband width to AR width ratio r depending on the AR mean near-surface temperature T_m and the mean crossing latitude ϕ_m. Color coding in Fig. 4 splits the data points with respect to the median values of $T_m = 287.5$ K and $\phi_m = 40°$N with red symbols corresponding to the warmer AR events (in Fig. 4a) or more southern satellite AR crossings (in Fig. 4b), and the blue symbols representing the colder ones (in Fig. 4a) or more northern crossings (in Fig. 4b). It can be seen that for colder and more northern events (compared to warmer and more southern events) there is some trend of diminishing r as IWV$_m$ increases. The mean values of the ratio r for events with $T_m \leq 287.5$ K or $\phi_m \geq 40°$N and $T_m > 287.5$ K or $\phi_m < 40°$N are 0.63–0.66 and 0.26–0.29, respectively. As for precipitation regime partitioning and mean rain rates for

different types of rainfall, the differences between estimates of r for cool seasons of different years were rather modest. For example, the mean values of r for all AR events within an individual season period were 0.43, 0.38, and 0.56 for the 2006–07, 2007–08, and 2008–09 observational periods, respectively.

As seen from the data scatter in Fig. 4, not only the ratio of the rainband width to the AR width r, but also the variability of this ratio generally decreases as IWV$_m$ increases. Larger IWV$_m$ values are expected for warmer and more southerly AR crossings. To illustrate this fact, Fig. 5 depicts the IWV$_m$–T_m and IWV$_m$–ϕ_m scatterplots for all AR observed crossings. The best fit linear approximations are given as

$$\text{IWV}_m(\text{mm}) = 0.94 T_m(\text{K}) - 241 \quad \text{and} \quad (1)$$

$$\text{IWV}_m(\text{mm}) = -0.31 \phi_m(°) + 42.8. \quad (2)$$

The correspondence between IWV$_m$ and T_m, however, is somewhat more direct compared to the IWV$_m$–ϕ_m correspondence as the correlation coefficient for the relation (1) is 0.56 as opposed to only 0.35 for the relation (2). Despite moderate correlations, there is a fair amount of IWV$_m$ data scatter for any given AR mean temperature T_m or the mean crossing latitude ϕ_m.

c. Positions of rainbands within ARs

Satellite observations from *CloudSat* and *Aqua* AMSR-E sensors indicate that boundaries of rainfall areas associated with atmospheric river events over the eastern North Pacific Ocean vary from crossing to crossing. Rainfall does not necessarily start as IWV reaches the 20-mm threshold, which is usually considered to be the AR boundary. There is, however, a noticeable correlation between the AR mean temperature near the surface T_m, and IWV at locations within a satellite crossing where rainfall starts and ends. For all the observed satellite crossings considered in this study, Fig. 6 shows the scatterplots of between T_m (and also mean crossing latitude ϕ_m) and the values of IWV at the southern and
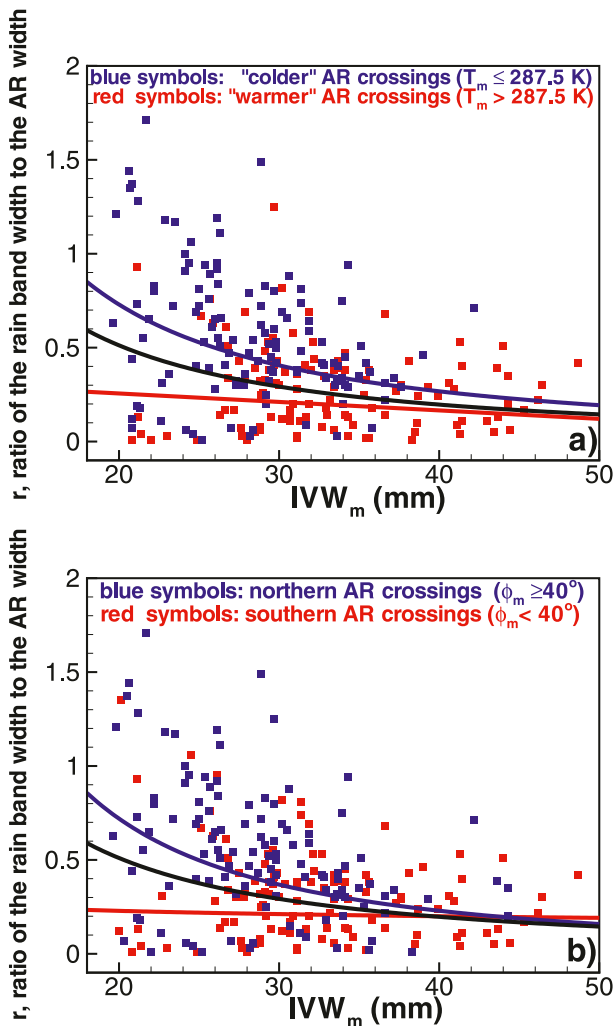
FIG. 4. The ratio of the rainband width to the AR width as a function of the mean value of IWV stratified with respect to the (a) AR temperature near the surface T_m and (b) mean latitude of AR crossings ϕ_m. For the entire dataset blue, red, and black curves show mean trends for colder [in (a), $T_m \leq 287.5\,\text{K}$] and more northern crossings [in (b), $\phi_m \geq 40°$], warmer [in (a), $T_m > 287.5\,\text{K}$] and more southern crossings [in (b), $\phi_m < 40°$], and all ARs events correspondingly.

FIG. 5. The scatterplots between IWV$_m$ and (a) the mean AR temperature near the surface T_m and (b) a mean latitude of an AR crossing ϕ_m for the entire 2006–09 dataset.

northern extents of rainbands within a crossing (IWV$_s$ and IWV$_n$), correspondingly.

It can be seen from Fig. 6a that the start of rainfall at the AR southern boundary is more likely to happen when IWV$_s$ values are higher than 20 mm. Very few data points (about 2% of the total amount) indicate the start of rainfall at IWV$_s < 20$ mm. For warmer events ($T_m > 290$ K), it is not unusual that rainfall did not start until IWV$_s$ is relatively large, reaching 40 mm and even higher values. The correlation coefficient between IWV$_s$ and T_m is 0.44, which reflects moderate correlation between these parameters. The best-fit linear relation is given by
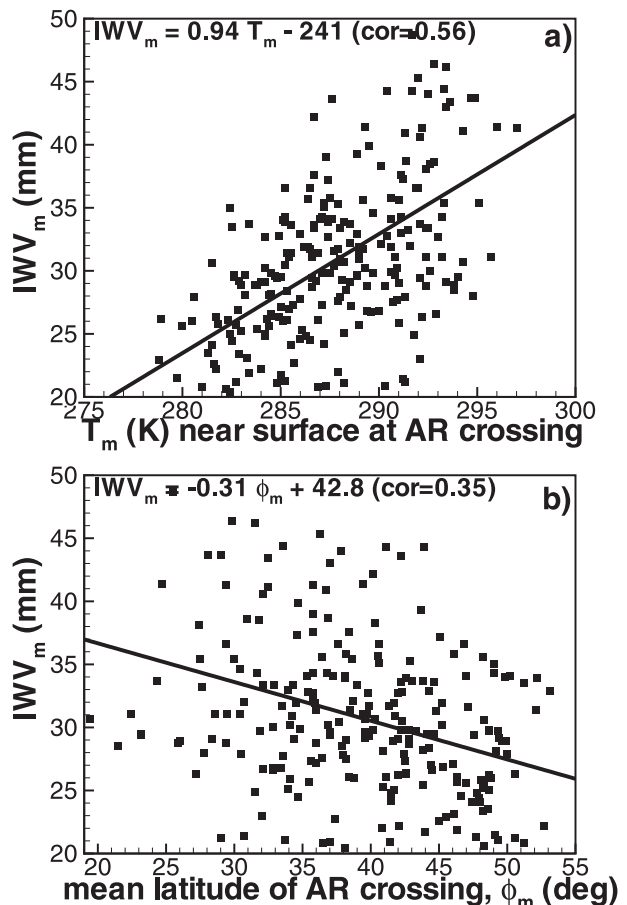
$$IWV_s(\text{mm}) = 0.70T_m(\text{K}) - 171. \qquad (3)$$

An average relation between IWV$_s$ and mean crossing latitude ϕ_m is shown in Fig. 6b and is described by the linear fit:

$$IWV_s(\text{mm}) = 40.0 - 0.227\phi_m. \qquad (4)$$

The correlation coefficient between IWV$_s$ and ϕ_m is, however, noticeably smaller (i.e., 0.26) compared to that describing the relation (3).

At the northern AR boundary, rainfall ends at IWV$_n$ values that are generally less than IWV$_s$ values. For colder and more northern AR crossings rainfall can be observed down to IWV$_n$ values that are as low as 12–15 mm. For 26% of the AR crossings, rainfall ends at IWV$_n < 20$ mm. Compared to the IWV$_s$–T_m pair, there is a somewhat stronger correlation between IWV$_n$ and T_m (i.e., 0.73 versus 0.44). The corresponding best linear fit is
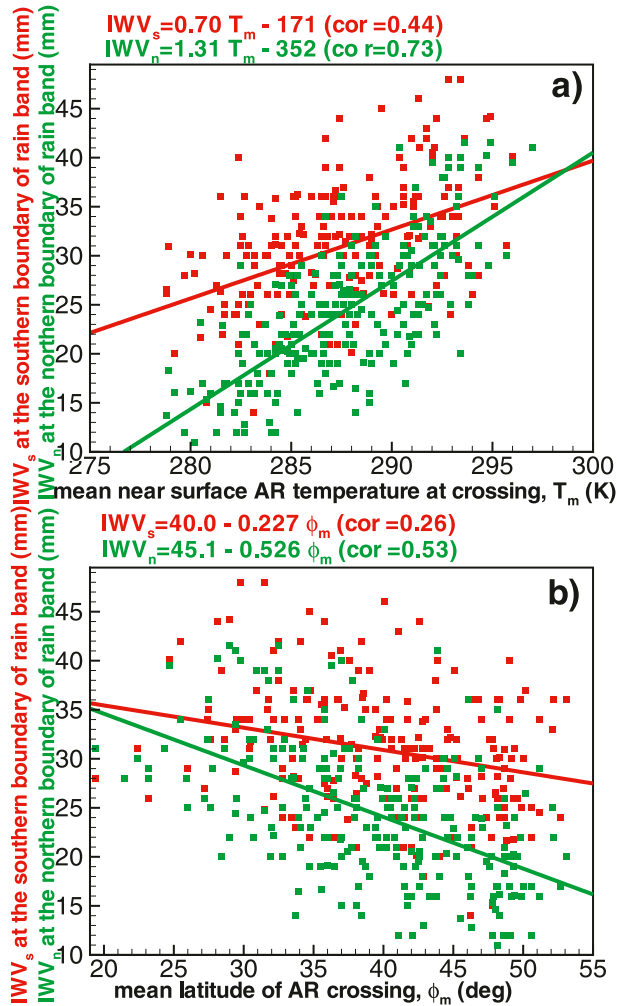
FIG. 6. The scatterplots between IWV at southern (IWV_s) and northern (IWV_n) boundaries of (a) rainbands associated with AR and AR mean temperature near the surface T_m and (b) a mean latitude of an AR crossing ϕ_m, as obtained from the entire 2006 to 2009 dataset.

$$IWV_n(mm) = 1.31 T_m(K) - 352. \quad (5)$$

As for southern-integrated water vapor boundaries of rainfall bands, IWV_n values show less correlation with ϕ_m than with T_m (0.53 versus 0.73). A corresponding linear fit between IWV_n and ϕ_m is given by

$$IWV_n(mm) = 45.1 - 0.526\phi_m. \quad (6)$$

There are no significant differences between the results for the entire dataset and the results for the cool season observation periods of individual years (not shown).

d. Water substance partitioning in cold rainfall

Ice/snowflake particle melting is the primary precipitation formation process for cold rainfall, which is often of the stratiform type and produces the radar BB features identifying the freezing level. *CloudSat* retrievals of ice mass above the freezing level and independent estimates of rain rate below this level can be used for constructing observationally based relations between parameters of precipitating ice and resultant rainfall. Such relations can be helpful for validating microphysical parameterization schemes in different models.

The total ice mass in the vertical atmospheric column is characterized by IWP, which is obtained by vertically integrating values of IWC retrieved from *CloudSat* measurements above the freezing level. Relating IWP and mean rain rate R in the liquid hydrometeor layer, which are obtained for the same atmospheric column (i.e., from one vertical profile of CPR measurements), indicates a certain correlation between these parameters (e.g., Matrosov 2012). Effects of wind shear and horizontal advection, however, may cause decorrelation between IWP and R derived from one-column measurements. It is hypothesized that the role of these effects is subdued if the AR crossing mean ice water path and rain-rate values (i.e., IWP_m and R_m) instead of individual profile values are used. The relatively large number of AR crossings analyzed in this study enables consideration to be taken of the relations between total ice mass and rain rate in terms of the crossing mean values of IWP_m and R_m.

Figure 7 shows the IWP_m and R_m scatterplots for individual year observation periods (Figs. 7a–c) and also for the entire 2006–09 dataset (Fig. 7d). In the case when mixed rainfall was observed during an AR crossing, the data shown represent the cold rain fraction of this particular crossing. While the uncertainties of IWC values retrieved from *CloudSat* measurements could be as high as 50%–70% for individual IWC points (Matrosov and Heymsfield 2008), it is believed that uncertainties of IWP estimates are less than those for IWC due to partial canceling out of random components of the IWC retrieval errors as a result of vertical integration.

As seen from Fig. 7, IWP_m values of precipitating systems associated with AR events vary from a few hundred grams per square meter to several kilograms per square meter. IWP values for individual CPR measurement profiles can reach $10\,kg\,m^{-2}$ (not shown). There is a moderate correlation between IWP_m and R_m. The best-fit power-law relations are also shown in Fig. 7. The corresponding correlation coefficients are 0.71, 0.62, 0.67, and 0.68 for the 2006–07, 2007–08, 2008–09, and composite 2006–09 observational periods. As for the other AR parameters discussed above, there are no statistically significant differences between the IWP_m and R_m–correspondences depending on the choice of the observational cool season period.
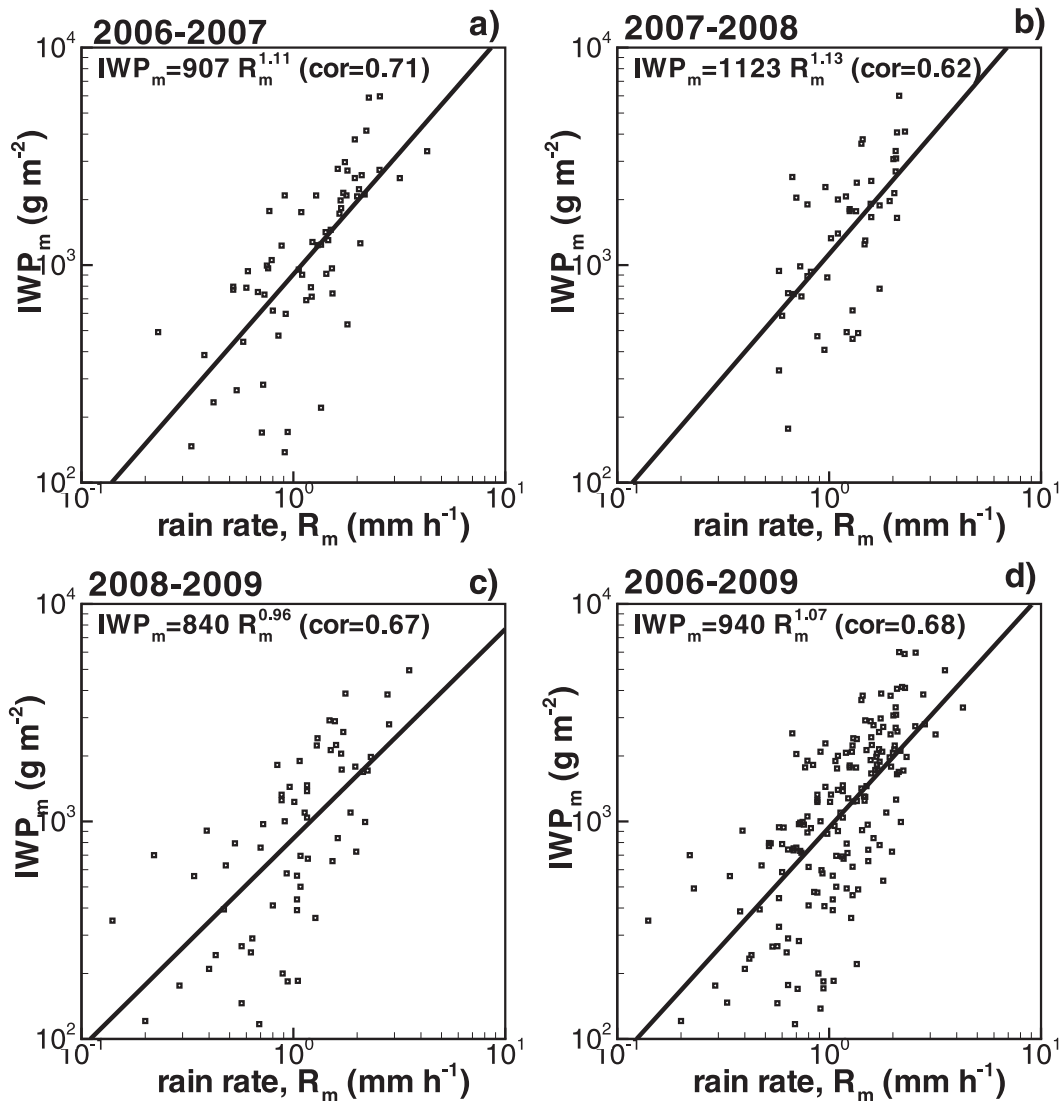
FIG. 7. Scatterplots between mean values of IWP and rain rate retrieved for the regions of cold rain observed at satellite AR crossings during (a) 2006–07, (b) 2007–08, (c) 2008–09, and (d) the entire observational period. Correlation coefficients and best-fit power-law approximations are also shown.

The presence of a reasonable correlation between ice amount aloft and the resultant rain rate for stratiform brightband precipitating systems is not surprising. For many years vertical profile of reflectivity (VPR) approaches have been used for quantitative precipitation estimation (QPE) from ground-based scanning radar measurements when the radar beam overshoots rain regions at longer ranges due to Earth's sphericity. Under these approaches, reflectivity measured aloft in precipitating ice regions is related in a quantitative sense to reflectivity/rain rate near the ground (e.g., Koistinen 1991). Since ice content retrievals and traditional radar QPE are based on reflectivity measurements, VPR QPE approaches are, to a certain degree, based on empirical

relations between the ice amount aloft and the resultant rain rate. *CloudSat* measurements allowed for independent estimations of such relations in terms of precipitating ice and the resultant rain.

4. Conclusions

In this study simultaneous spaceborne observations of the atmospheric rivers (ARs) over the eastern North Pacific Ocean from different sensors aboard the A-Train satellite formation were analyzed. The dataset consisted of measurements conducted during three consecutive cool seasons (October–March) from 2006 to 2009 when ARs are most active and affect the West Coast of North

America, usually causing abundant precipitation and sometimes flooding. During the aforementioned observation period, there were 265 satellite AR crossings for which measurements existed.

The AR rainfall and precipitating ice cloud parameters were independently retrieved from the *CloudSat* W-band nadir-pointing radar, while the AR IWV values and boundaries (using the conventional 20-mm integrated water vapor threshold) were simultaneously determined from passive microwave measurements by the AMSR-E sensor aboard the *Aqua* satellite. For the AR events analyzed in this study, there was a moderate correlation between the mean value of IWV and the average AR temperature at the surface near satellite crossings.

Although precipitation was present for practically all observed AR satellite crossings including areas within and beyond AR boundaries, the extent of the rainfall regions varied significantly. The mean ratios of the rainband width to the AR width were about 0.4–0.5 with diminishing trends as AR events become warmer, which generally corresponds to more southerly AR crossings. A similar latitudinal dependence was found by Ralph et al. (2004), who used solely passive microwave retrievals. Colder events were characterized by greater variability of rainband widths. The northern and southern boundaries of the rainbands were noticeably correlated with the mean AR temperature near the surface. Corresponding correlations of these boundaries with mean latitudes of AR satellite crossings were less pronounced. While at its southern edge rainfall associated with ARs usually started at the IWV values exceeding 20 mm, precipitation regions often extended beyond northern AR boundaries.

Different precipitation regimes were observed in the AR events analyzed in this study. These regimes include "cold" rainfall (i.e., precipitation with ice regions above the freezing level often accompanied by the radar brightband features caused by ice melting, "warm" rainfall, i.e., precipitation typically restricted to temperatures above freezing with limited amounts of ice), and regions of mixed precipitation when both warm and cold rainfall types were observed during one AR crossing. Predominantly warm or cold rainfall was observed, on average, in two-thirds (one-third each) of the events, with the remaining events being of the mixed type. The fraction of the cold rainfall, however, increases with a decrease of the AR temperature, which generally corresponds to more northern AR crossings. Mean rain rates of precipitation associated with ARs were about 0.5, 1.5, and 1 mm h^{-1}, for warm, cold, and mixed rainfall events, respectively; although for individual events, the precipitation intensity could be more significant.

Independent estimates of the total ice phase amount and rainfall intensity from *CloudSat* measurements for cold precipitation regions of ARs revealed a significant correlation between event mean values of columnar ice water passage and the resultant rain rate R_m. The corresponding correlation coefficients were approximately 0.6–0.7. The total amount of columnar ice typically varied from several hundred grams to several kilograms per square meter.

While AR satellite observations were conducted during three different cold seasons that were characterized by different phases of El Niño–Southern Oscillation, the dataset on AR properties analyzed in this study did not reveal any statistically significant differences depending on the ENSO phase. No significant differences in AR properties considered here were found based on the regions where ARs connected to the moisture reservoirs at low latitudes.

REFERENCES

Dettinger, M., 2011: Climate change, atmospheric rivers, and floods in California—A multimodel analysis of storm frequency and magnitude changes. *J. Amer. Water Resour. Assoc.,* **47,** 514–523.

Guan, B., N. P. Molotoch, D. E. Waliser, E. J. Fetzer, and P. J. Neiman, 2010: Extreme snowfall events linked to atmospheric rivers and surface air temperature via satellite measurements. *Geophys. Res. Lett.,* **37,** L20401, doi:10.1029/2010GL044696.

Haynes, J. M., T. S. L'Ecuyer, G. L. Stephens, S. D. Miller, C. Mitrescu, N. B. Wood, and S. Tanelli, 2009: Rainfall retrieval over the ocean with spaceborne W-band radar. *J. Geophys. Res.,* **114,** D00A22, doi:10.1029/2008JD009973.

Jankov, I., J. W. Bao, P. J. Neiman, P. J. Schultz, H. Yuan, and A. B. White, 2009: Evaluation and comparisons of microphysical algorithm in ARW-WRF model simulations of atmospheric river events affecting California coast. *J. Hydrometeor.,* **10,** 847–870.

Koistinen, J., 1991: Operational correction of radar rainfall errors due to the vertical reflectivity profile. Preprints, *25th Int. Conf. on Radar Meteorology,* Paris, France, Amer. Meteor. Soc., 91–94.

Lavers, D. A., R. P. Allan, E. F. Wood, G. Villarini, D. J. Brayshaw, and A. J. Wade, 2011: Winter floods in Britain are connected to atmospheric rivers. *Geophys. Res. Lett.,* **38,** L23803, doi:10.1029/2011GL049783.

Leung, L. R., and Y. Qian, 2009: Atmospheric rivers induced heavy precipitation and flooding in the western U.S. simulated by the WRF regional climate model. *Geophys. Res. Lett.,* **36,** L003820, doi:10.1029/2008GL036445.

Matrosov, S. Y., 1997: Variability of microphysical parameters in high altitude ice clouds: Results of the remote sensing method. *J. Appl. Meteor.,* **36,** 633–648.

——, 2007: Potential for attenuated-based estimations of rainfall rate from CloudSat. *Geophys. Res. Lett.,* **34,** L05817, doi:10.1029/2006GL029161.

——, 2008: Assessment of radar signal attenuation caused by the melting hydrometeor layer. *IEEE Trans. Geosci. Remote Sens.,* **46,** 1039–1047.

——, 2012: Observations of wintertime U.S. west coast precipitating systems with W-band satellite radar and other spaceborne instruments. *J. Hydrometeor.,* **13,** 223–238.

——, and A. J. Heymsfield, 2008: Estimating ice content and extinction in precipitating cloud systems from CloudSat radar measurements. *J. Geophys. Res.,* **113,** D00A05, doi:10.1029/2007JD009633.

——, A. Battaglia, and P. Rodriguez, 2008: Effects of multiple scattering on attenuation-based retrievals of stratiform rainfall from CloudSat. *J. Atmos. Oceanic Technol.,* **25,** 2199–2208.

Neiman, P. J., F. M. Ralph, G. A. Wick, Y.-H. Kuo, T. K. Wee, Z. Ma, G. H. Taylor, and M. D. Dettinger, 2008: Diagnosis of an intense atmospheric river impacting the Pacific Northwest: Storm summary and offshore vertical structure observed with COSMIC satellite retrievals. *Mon. Wea. Rev.,* **136,** 4398–4420.

Ralph, F. M., P. J. Neiman, and G. A. Wick, 2004: Satellite and CALJET aircraft observations of atmospheric rivers over the eastern North Pacific Ocean during the winter of 1997/98. *Mon. Wea. Rev.,* **132,** 1721–1745.

——, ——, ——, S. I. Gutman, M. D. Dettinger, D. R. Cayan, and A. B. White, 2006: Flooding on California's Russian River: Role of atmospheric rivers. *Geophys. Res. Lett.,* **33,** L112811, doi:10.1029/2006GL026669.

——, E. Sukovich, D. Reynolds, M. Dettinger, S. Weagle, W. Clark, and P. J. Neiman, 2010: Assessment of extreme quantitative precipitation forecasts and development of regional extreme event thresholds using data from HMT-2006 and COOP observers. *J. Hydrometeor.,* **11,** 1288–1306.

Schlüssel, P., and W. J. Emery, 1990: Atmospheric water vapour over oceans from SSM/I measurements. *Int. J. Remote Sens.,* **11,** 753–766.

White, A. B., P. J. Neiman, F. M. Ralph, D. E. Kingsmill, and P. O. G. Persson, 2003: Coastal orographic rainfall processes observed by radar during the California Land-Falling Jets Experiment. *J. Hydrometeor.,* **4,** 264–282.

Wick, G. A., Y.-H. Kuo, F. M. Ralph, T.-K. Wee, and P. J. Neiman, 2008: Intercomparison of integrated water vapor retrievals from SSM/I and COSMIC. *Geophys. Res. Lett.,* **35,** L21805, doi:10.1029/2008GL035126.

Zhu, Y., and R. E. Newell, 1998: A proposed algorithm for moisture fluxes from atmospheric rivers. *Mon. Wea. Rev.,* **126,** 725–735.